

# Pure-water-fed, electrocatalytic CO<sub>2</sub> reduction to ethylene beyond 1,000 h stability at 10 A

Received: 7 February 2023

Accepted: 13 November 2023

Published online: 5 January 2024

Check for updates

Xiaojie She<sup>1,5</sup>, Lingling Zhai<sup>1,5</sup>, Yifei Wang<sup>2,5</sup>, Pei Xiong<sup>1</sup>, Molly Meng-Jung Li<sup>1</sup>, Tai-Sing Wu<sup>3</sup>, Man Chung Wong<sup>1</sup>, Xuyun Guo<sup>1</sup>, Zhihang Xu<sup>1</sup>, Huaming Li<sup>4</sup>, Hui Xu<sup>4</sup>✉, Ye Zhu<sup>1</sup>✉, Shik Chi Edman Tsang<sup>2</sup>✉ & Shu Ping Lau<sup>1</sup>✉

Electrocatalytic CO<sub>2</sub> reduction at near-ambient temperatures requires a complex inventory of protons, hydroxyls, carbonate ions and alkali-metal ions at the cathode and anode to be managed, necessitating the use of ion-selective membranes to regulate pH. Anion-exchange membranes provide an alkaline environment, allowing CO<sub>2</sub> reduction at low cell voltages and suppression of hydrogen evolution while maintaining high conversion efficiencies. However, the local alkaline conditions and the presence of alkali cations lead to problematic carbonate formation and even precipitation. Here we report a pure-water-fed (alkali-cation-free) membrane-electrode-assembly system for CO<sub>2</sub> reduction to ethylene by integrating an anion-exchange membrane and a proton-exchange membrane at the cathode and anode side, respectively, under forward bias. This system effectively suppresses carbonate formation and prevents salt precipitation. A scaled-up electrolyser stack achieved over 1,000 h stability without CO<sub>2</sub> and electrolyte losses and with 50% Faradaic efficiency towards ethylene at a total current of 10 A.

Producing high-value chemicals and feedstocks from electrocatalytic CO<sub>2</sub> reduction (ECO<sub>2</sub>R) powered by sustainable energy could close the carbon loop and mitigate greenhouse gas emissions<sup>1,2</sup>. Much of the research effort in this regard has focused on optimizing the product selectivity, that is, the Faradaic efficiency (FE), of the catalysts for ECO<sub>2</sub>R, increasing their productivity (current density) and lowering the overpotentials of the reduction reactions<sup>3-7</sup>. However, optimizing only the catalytic module in the ECO<sub>2</sub>R system often does not translate into better overall system performance in large-scale reactors, where system stability is a major concern. The short lifespan of ECO<sub>2</sub>R is partially caused by carbonate precipitation and crossover accompanied

by electrolyte loss, resulting in additional energy consumption and CO<sub>2</sub> loss<sup>8</sup>.

Currently, most ECO<sub>2</sub>R systems include alkali-metal electrolytes (for example, KHCO<sub>3</sub>, KOH) (Supplementary Fig. 1) because alkali-metal cations accelerate ECO<sub>2</sub>R reaction kinetics, whose activity trend follows the sequence Cs<sup>+</sup> > K<sup>+</sup> > Na<sup>+</sup> > Li<sup>+</sup> (ref. 9). However, the local alkaline cathode condition can lead to carbonate formation, while introducing alkali-metal cations can even result in salt precipitation, complicating the electrolysis system and causing unstable overall system performance. For example, in the membrane-electrode-assembly (MEA) cell, the local alkaline cathode condition causes a major fraction of the

<sup>1</sup>Department of Applied Physics, Research Institute for Smart Energy, The Hong Kong Polytechnic University, Hong Kong, P. R. China. <sup>2</sup>Wolfson Catalysis Centre, Department of Chemistry, University of Oxford, Oxford, UK. <sup>3</sup>National Synchrotron Radiation Research Centre, Hsinchu, Taiwan. <sup>4</sup>Institute for Energy Research, School of the Environment and Safety Engineering, Jiangsu University, Zhenjiang, P. R. China. <sup>5</sup>These authors contributed equally: Xiaojie She, Lingling Zhai, Yifei Wang. ✉e-mail: [xh@ujs.edu.cn](mailto:xh@ujs.edu.cn); [yezhu@polyu.edu.hk](mailto:yezhu@polyu.edu.hk); [edman.tsang@chem.ox.ac.uk](mailto:edman.tsang@chem.ox.ac.uk); [apsplau@polyu.edu.hk](mailto:apsplau@polyu.edu.hk)

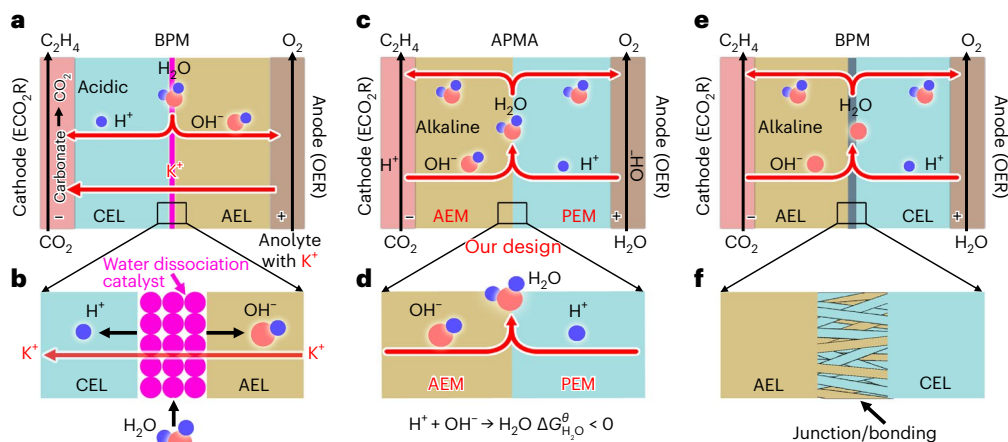


**Fig. 1 | A comparison of different electrolysis systems for  $\text{ECO}_2\text{R}$ .** a, b, The BPM system (a) and reaction (b) with an acidic cathode environment in reverse bias mode. c, d, The APMA system (c) and reaction (d) with an alkaline cathode

environment in forward bias mode. e, f, The commercial BPM system (e) and reaction (f) with a bipolar junction/bonding at the AEL/CEL interface in forward bias mode.

input  $\text{CO}_2$  to react with the electrogenerated  $\text{OH}^-$  to produce carbonate<sup>10–12</sup> (Supplementary Note 1 and Supplementary Fig. 1). Alkali cations can diffuse across the anion-exchange membrane (AEM) to the outer Helmholtz plane of the cathode, and anions (for example,  $\text{CO}_3^{2-}$ ,  $\text{HCO}_3^-$ ,  $\text{HCOO}^-$  and  $\text{CH}_3\text{COO}^-$ ) can be transported to the anode to release  $\text{CO}_2$  and be re-oxidized to  $\text{CO}_2$  (refs. 9,13,14 and Supplementary Fig. 1). This process not only results in  $\text{CO}_2$  and product losses but also gradually increases the cell voltage and even could consume up to ~70% of the energy input for  $\text{ECO}_2\text{R}$  to  $\text{C}_2\text{H}_4$  (ref. 15,16). Thus, so far, the system stability of  $\text{ECO}_2\text{R}$  to  $\text{C}_2\text{H}_4$  in the flow and MEA cells has generally been less than 200 h (Supplementary Fig. 2 and Supplementary Table 1).

In this Article, we describe the design of an AEM + proton-exchange membrane (PEM) assembly (APMA) MEA system with pure  $\text{H}_2\text{O}$  as the anolyte to suppress/prevent carbonate formation/precipitation. The AEM interfaces with the cathode in the APMA system to provide an alkaline cathode environment for  $\text{ECO}_2\text{R}$ . The introduced PEM in contact with the anode can effectively prevent the crossover of all anions. More importantly, the membrane configuration and pure  $\text{H}_2\text{O}$  anolyte suppress the reaction of  $\text{CO}_2$  with the electrogenerated  $\text{OH}^-$  to form carbonate and salt precipitation. We employed a commercially available AEM and PEM to construct the pure- $\text{H}_2\text{O}$ -fed (alkali-cation-free) APMA-MEA architecture, which was assembled with high-performance surface-step-rich Cu (SS-Cu) for  $\text{ECO}_2\text{R}$  to  $\text{C}_2\text{H}_4$ . In situ Raman spectra and isotope labelling experiments revealed that carbonate formation can be effectively suppressed in the pure- $\text{H}_2\text{O}$ -fed APMA system rather than regenerating  $\text{CO}_2$  from carbonate. As a result of suppressing carbonate formation/precipitation and anion crossover,  $\text{ECO}_2\text{R}$  to  $\text{C}_2\text{H}_4$  could operate continuously for over 1,000 h without  $\text{CO}_2$  or electrolyte losses in a pure- $\text{H}_2\text{O}$ -fed six-APMA-MEA cell stack while achieving a  $\text{C}_2\text{H}_4$ -specific FE of 50% at 10 A.

### Design of the APMA system

Currently, the use of PEM and bipolar membrane (BPM) systems with an acidic cathode environment can eliminate carbonate formation by regenerating  $\text{CO}_2$  from carbonate to some extent<sup>11,12,17–19</sup> (Supplementary Fig. 1), but the diffusion of alkali-metal cations from the anolyte under the electric field causes electrolyte loss and the acidic cathode environment also results in a lower product FE owing to the more thermodynamically favourable hydrogen evolution reaction (HER)<sup>9,20</sup>. Furthermore, the BPM MEA system needs to have the cation-exchange layer (CEL) and anion-exchange layer (AEL) in contact with the cathode and the anode, respectively<sup>12,17,21,22</sup> (Fig. 1a). Under reverse bias (Supplementary Note 1), water dissociation occurs at the CEL/AEL interface<sup>23</sup>,

with  $\text{H}^+/\text{OH}^-$  driven through CEL/AEL to take part in the  $\text{ECO}_2\text{R}$ /oxygen evolution reaction (OER). Usually, the water dissociation catalyst (for example,  $\text{TiO}_2$  or  $\text{Al}(\text{OH})_3$ ) must be assembled at the CEL/AEL interface to lower the water dissociation overpotential<sup>24–26</sup> (Fig. 1b). However, in this configuration, the BPM is easily delaminated, which can result in a catastrophic degradation of the cell stability.

Despite the benefits of the alkali environment and the alkali cations for the  $\text{CO}_2$  reduction kinetics in AEM, PEM and BPM systems, they show inferior system performance (see Supplementary Note 1 for details). Thus, it is highly desirable to perform  $\text{ECO}_2\text{R}$  in alkali-cation-free media while maintaining an alkali cathode environment. Consequently, we designed an APMA-MEA system with pure  $\text{H}_2\text{O}$  as the anolyte to suppress/prevent carbonate formation/precipitation (Fig. 1c). Importantly, the AEM interfaces with the cathode in the APMA system to provide an alkaline cathode environment since the AEM contains abundant  $\text{OH}^-$  (refs. 23,27). In contrast to the previous BPM system<sup>12,17,26</sup> (Fig. 1a), the APMA does not include a water dissociation catalyst, as water dissociation occurs at the cathode and anode, and the produced  $\text{OH}^-$  and  $\text{H}^+$  can spontaneously form water at the interface (standard Gibbs free energy change,  $\Delta G_{\text{H}_2\text{O}}^\ominus < 0$ ; Fig. 1d), and the formed  $\text{H}_2\text{O}$  can pass through the AEM/PEM to the cathode/anode. The introduced PEM can effectively prevent the crossover of all anions, and the APMA and pure  $\text{H}_2\text{O}$  anolyte can suppress the reaction of  $\text{CO}_2$  with the electrogenerated  $\text{OH}^-$  to form salt/precipitation under the influence of the electrostatic field (see below). In principle, the commercial BPM can also meet our APMA system requirements (Fig. 1e). However, the current BPM technology is immature, making its performance vary greatly. The BPM usually has the junction/bonding layer at the AML/CEL interface (Fig. 1f). The water formation at the interface may result in delamination and lead to instability of the BPM due to the difficulty in controlling the mechanical strength of the junction/bonding. In light of the above, the commercially available AEM and PEM were used to construct our APMA system.

### Synthesis and characterizations of the SS-Cu catalyst

SS-Cu nanoparticles (with an average diameter of ~60 nm) with abundant stacking faults and grain boundaries were prepared by a facile solution method (Fig. 2a and Supplementary Figs. 3 and 4). The stacking faults and grain boundaries favour higher  $\text{ECO}_2\text{R}$  activity<sup>3,28–30</sup>. High-resolution transmission electron microscopy (HRTEM) and aberration-corrected high-angle annular dark-field (HAADF) scanning TEM (STEM) images revealed abundant stacking faults that intersect with each other (Fig. 2b and Supplementary Fig. 3) and multitudinous, interlaced grain boundaries (Fig. 2c) in SS-Cu. Furthermore,

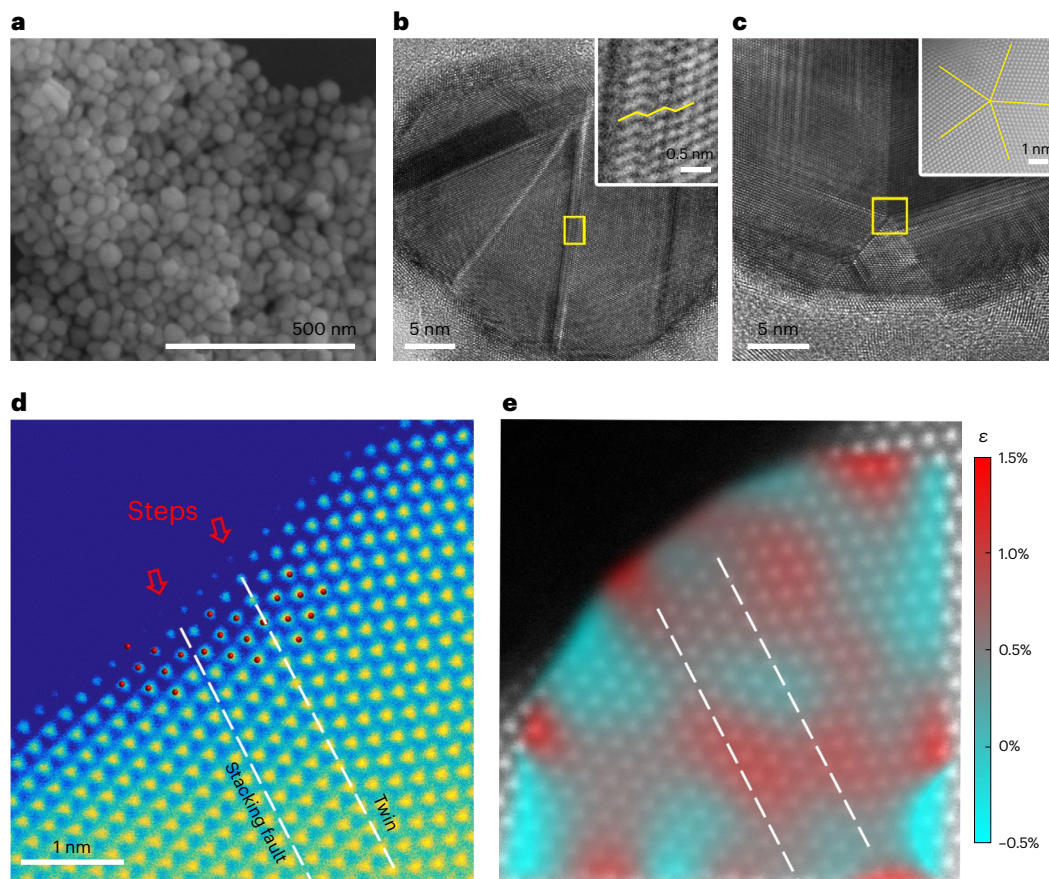


**Fig. 2 | Microstructural characterizations of SS-Cu.** **a**, A scanning electron microscopy image of SS-Cu. **b,c**, Typical HRTEM images of SS-Cu, revealing abundant stacking faults (**b**) and grain boundaries (**c**) with inset atomic-resolution HAADF-STEM images from the area highlighted with a yellow rectangle. The yellow lines in the insets highlight stacking faults and five-fold twin boundaries. **d**, An atomic-resolution HAADF-STEM image showing stepped

faces induced by a stacking fault and a twin boundary, both along {111} planes (dashed white lines). **e**, GPA strain ( $\epsilon$ ) mapping on **d**, showing tensile strain near the surface exits of the stacking fault and the twin boundary, using the lattice far from these defects as a reference (zero strain). The measured strain is perpendicular to the {111} plane along which the stacking fault and twin boundary align.

grain boundaries contain  $\Sigma 3$  coincident site lattice boundaries (twin boundaries) and form some typical five-fold twinning structures (Fig. 2c, inset and Supplementary Fig. 5). These abundant stacking faults and grain boundaries can induce sizeable tensile strain on the surface layer<sup>3,30,31</sup>. Indeed, a significant local tensile strain as large as  $\sim 0.8\%$  was observed around the surface exits of both twin boundaries and stacking faults in SS-Cu by geometric-phase analysis (GPA) (Fig. 2d,e and Supplementary Fig. 6), compared with that of a defect-free Cu lattice (Supplementary Fig. 7). Furthermore, stepped surfaces were also induced at the surface exits of twin boundaries and stacking faults (Fig. 2d and Supplementary Fig. 6), giving rise to surface Cu atoms with low coordination number (see Supplementary Note 2 for more information about SS-Cu, as well as Supplementary Videos 1 and 2, Supplementary Figs. 8–19 and Supplementary Table 2).

### ECO<sub>2</sub>R performance in the conventional flow cell

Upon successfully obtaining the SS-Cu catalyst, we first evaluated its ECO<sub>2</sub>R performance in a flow cell with the conventional alkaline condition (1 M KOH). SS-Cu delivered a peak FE of  $\sim 80\%$  towards C<sub>2</sub>H<sub>4</sub> at about  $-0.58$  V (stated versus a reversible hydrogen electrode (RHE) throughout the text, unless otherwise noted), at which  $j_{\text{C}_2\text{H}_4}$  reached  $\sim 568$  mA cm<sup>-2</sup> and the half-cell energy efficiency (EE<sub>half cell</sub>) of C<sub>2</sub>H<sub>4</sub> was up to  $\sim 51\%$  (Fig. 3a,c and Supplementary Fig. 20). Compared with the current best ECO<sub>2</sub>R-to-C<sub>2</sub>H<sub>4</sub> performance in 1 M KOH (FE<sub>C<sub>2</sub>H<sub>4</sub></sub> of  $\sim 80\%$  and  $j_{\text{C}_2\text{H}_4}$  of 400–480 mA/cm<sup>2</sup>, at about  $-1.5$  V)<sup>5</sup>, SS-Cu delivered a  $\sim 1.3$  times higher  $j_{\text{C}_2\text{H}_4}$  and a  $\sim 2.6$  times lower potential. Interestingly,

we found that the partial current density ( $j_{\text{C}_2\text{H}_4}$ ,  $j_{\text{C}_2\text{H}_4}$  or  $j_{\text{without H}_2}$ ) showed a strong linear correlation with the function of the tensile strain and coordination number (see Supplementary Note 3 and Supplementary Figs. 21–35 for details).

To eliminate carbonate formation, precipitation and crossover in the AEM cell during ECO<sub>2</sub>R, we also performed ECO<sub>2</sub>R over SS-Cu in strong acid (pH < 1) to regenerate CO<sub>2</sub> from the formed carbonate<sup>11</sup>. Under the strongly acidic catholyte with abundant K<sup>+</sup>, the system delivered barely satisfactory ECO<sub>2</sub>R-to-C<sub>2</sub>H<sub>4</sub> performance (FE<sub>C<sub>2</sub>H<sub>4</sub></sub> of  $\sim 48\%$  and FE<sub>C<sub>2</sub>H<sub>4</sub></sub> of  $\sim 33\%$  with  $j_{\text{total}}$  of  $-345$  mA cm<sup>-2</sup> at  $-1.1$  V) in a PEM assembled flow cell (Fig. 3b,d; see Supplementary Note 4 and Supplementary Figs. 36–38 for details). Considering practical viability, we sought to operate ECO<sub>2</sub>R in the PEM-MEA cell with an acidic cathode environment (just as in Supplementary Fig. 1). The anolyte with K<sup>+</sup> was used not only as the proton resource but also to supply K<sup>+</sup> to the cathode. Although we initially observed formation of ECO<sub>2</sub>R products (such as CO and C<sub>2</sub>H<sub>4</sub>), ECO<sub>2</sub>R shut down after a few minutes, and HER became dominant. The continuous K<sup>+</sup> passed through the PEM from the anode to the cathode, accompanied by carbonate salt precipitation in the cell's flow channel, which blocked CO<sub>2</sub> mass transfer (Supplementary Note 4 and Supplementary Fig. 39).

### ECO<sub>2</sub>R performance in the pure-H<sub>2</sub>O-fed APMA system

On the basis of the results described above, we proposed a pure-H<sub>2</sub>O-fed (alkali-cation-free) MEA electrolysis architecture, which is designed with the expectation that it can prevent carbonate formation/precipitation



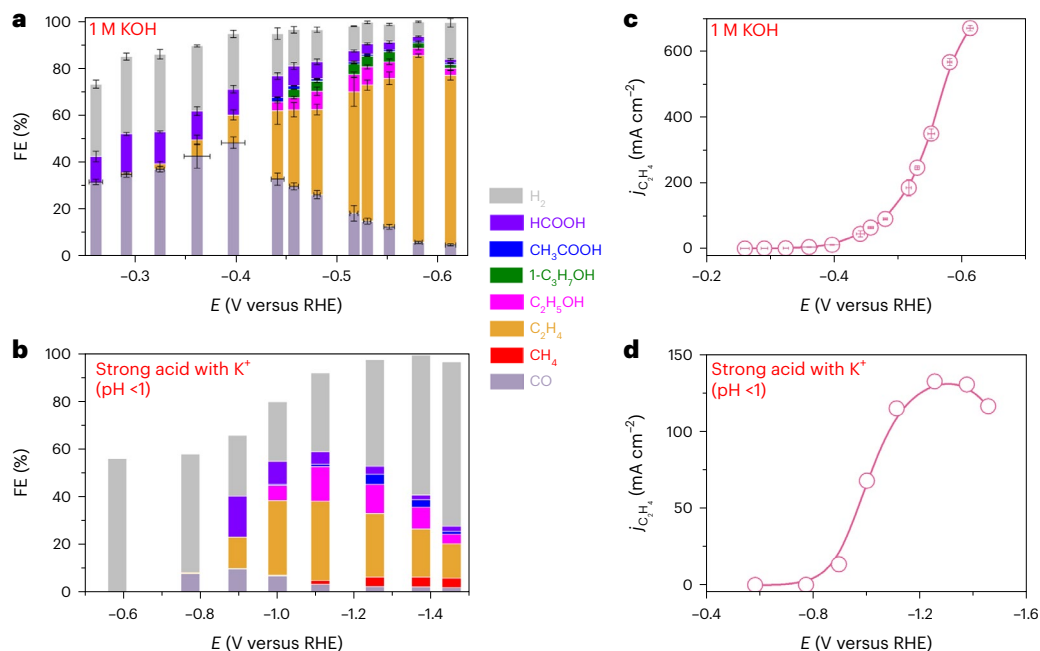
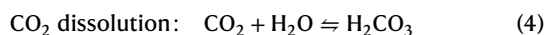
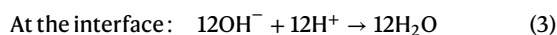
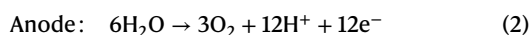
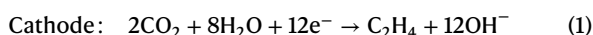


**Fig. 3 | The ECO<sub>2</sub>R performance of SS-Cu in the flow cell with 1 M KOH/strong acid as the electrolyte. a, b**, The FEs towards ECO<sub>2</sub>R products under a range of applied potentials under 1 M KOH (a) and 1 M H<sub>3</sub>PO<sub>4</sub> containing 3 M KI as the catholyte and 1 M H<sub>3</sub>PO<sub>4</sub> as the anolyte (b), respectively. **c, d**, The partial current

densities of C<sub>2</sub>H<sub>4</sub> under a range of applied potentials under 1 M KOH (c) and 1 M H<sub>3</sub>PO<sub>4</sub> containing 3 M KI as the catholyte and 1 M H<sub>3</sub>PO<sub>4</sub> as the anolyte (d), respectively. Values are means, and error bars indicate the s.d. (*n* = 3 replicates).

and anion crossover. The central concept of the pure-H<sub>2</sub>O-fed MEA system for ECO<sub>2</sub>R is maintaining the alkaline cathode environment necessary for effective ECO<sub>2</sub>R to multicarbon products<sup>27,32</sup>. Thus, we constructed an APMA, which was encompassed in the MEA architecture held under pressure to prevent delamination and to ensure uniform contact between the gas diffusion electrodes (GDEs) and membranes (Fig. 4a). The AEM in contact with the cathode can create an alkaline cathode environment, while the PEM facing the anode can circumvent the crossover of all anions, including anion products (such as HCOO<sup>-</sup> and CH<sub>3</sub>COO<sup>-</sup>).



Under forward bias, H<sub>2</sub>O dissociation occurs at the cathode and anode, participating in ECO<sub>2</sub>R and the OER (Fig. 1c). The remaining OH<sup>-</sup> at the cathode and H<sup>+</sup> at the anode can be transported through the AEM and PEM, respectively, forming H<sub>2</sub>O at their interface (equations (1)–(3)), which can pass through the AEM/PEM to the cathode/anode to re-participate in ECO<sub>2</sub>R or drain from the flow channel.

More importantly, in this APMA-MEA system architecture, the probability that the reactant CO<sub>2</sub> will react with the electrogenerated OH<sup>-</sup> to form salt precipitation (such as K<sub>2</sub>CO<sub>3</sub>) is drastically reduced (Supplementary Fig. 40). The thermodynamic explanation is that the pure H<sub>2</sub>O system can effectively suppress (bi)carbonate salt formation while the precipitation of salts (such as K<sub>2</sub>CO<sub>3</sub> or KHCO<sub>3</sub>) can be thoroughly prevented owing to the absence of cations under the influence of the electrostatic field. Furthermore, although a small amount of CO<sub>2</sub> can dissolve in H<sub>2</sub>O to form H<sub>2</sub>CO<sub>3</sub> (equation (4)), the alkaline cathode

environment and pure H<sub>2</sub>O anolyte can suppress H<sub>2</sub>CO<sub>3</sub> formation. The pure-H<sub>2</sub>O-fed APMA-MEA system suppresses/prevents carbonate formation/precipitation and anion crossover.

However, the pure H<sub>2</sub>O electrolysis system cannot avoid high operation voltage. For this pure-H<sub>2</sub>O-fed APMA-MEA system, the cell voltage can be conceptually decomposed into the following (equation (5)) (to simplify the calculation, we take ECO<sub>2</sub>R to C<sub>2</sub>H<sub>4</sub> as an example without considering the other products; see Supplementary Note 5 for details): the thermodynamic potential of ECO<sub>2</sub>R to C<sub>2</sub>H<sub>4</sub> in the alkaline environment and OER in H<sub>2</sub>O ( $E_{\text{CO}_2/\text{C}_2\text{H}_4}^{\theta, \text{base}} - E_{\text{O}_2/\text{H}_2\text{O}}^{\theta, \text{neutral}} = -1.98 \text{ V}$ ); the ECO<sub>2</sub>R-to-C<sub>2</sub>H<sub>4</sub> and OER overpotentials at a given current density ( $\delta_{\text{C}_2\text{H}_4}^{\text{base}}$  and  $\delta_{\text{OER}}^{\text{neutral}}$ ); the thermodynamic potential of H<sub>2</sub>O formation ( $E_{\text{H}_2\text{O}}^{\theta} = -\Delta G_{\text{H}_2\text{O}}^{\theta}/F = 0.83 \text{ V}$  at standard conditions due to the acidic and alkaline environments at the APMA interface); the overpotential of H<sub>2</sub>O formation ( $\delta_{\text{H}_2\text{O}}$ ); the voltage loss from the ohmic resistance ( $E_{\text{Ohm}}$ ); the voltage loss from the Nernst potential ( $E_{\text{Nernst loss}} = 0.058 \Delta \text{pH}$  at room temperature). Here,  $\delta_{\text{H}_2\text{O}}$ ,  $E_{\text{Ohm}}$  and  $E_{\text{Nernst loss}}$  are defined to be positive. Since CO is a crucial intermediate for C<sub>2</sub>H<sub>4</sub> formation and the thermodynamic potential of ECO<sub>2</sub>R to CO is more negative than that of ECO<sub>2</sub>R to C<sub>2</sub>H<sub>4</sub> (refs. 7,33–35),  $E_{\text{CO}_2/\text{CO}}^{\theta, \text{base}}$  was also calculated (Supplementary Note 5).

$$E_{\text{total}} = E_{\text{CO}_2/\text{C}_2\text{H}_4}^{\theta, \text{base}} - E_{\text{O}_2/\text{H}_2\text{O}}^{\theta, \text{neutral}} + \delta_{\text{C}_2\text{H}_4}^{\text{base}} - \delta_{\text{OER}}^{\text{neutral}} + E_{\text{H}_2\text{O}}^{\theta} - \delta_{\text{H}_2\text{O}} - E_{\text{Ohm}} - E_{\text{Nernst loss}} \quad (5)$$

$$E_{\text{Nernst loss}} = 2.303 \frac{RT}{zF} \log_{10} \frac{[\text{H}^+]_{\text{anode}}}{[\text{H}^+]_{\text{cathode}}} = 0.058 \Delta \text{pH} \quad (6)$$

where *R*, *T* and *z* are the ideal gas constant, temperature and ion valency, respectively. At room temperature (–25 °C), the ohmic resistance of the pure-H<sub>2</sub>O-fed APMA-MEA cell was very low (–0.88 Ω cm<sup>2</sup>) (Fig. 4b). However, when the current density is high,  $E_{\text{Ohm}}$  cannot be ignored (for example, at 100 mA cm<sup>–2</sup>,  $E_{\text{Ohm}} = -0.09 \text{ V}$ ). In addition, under

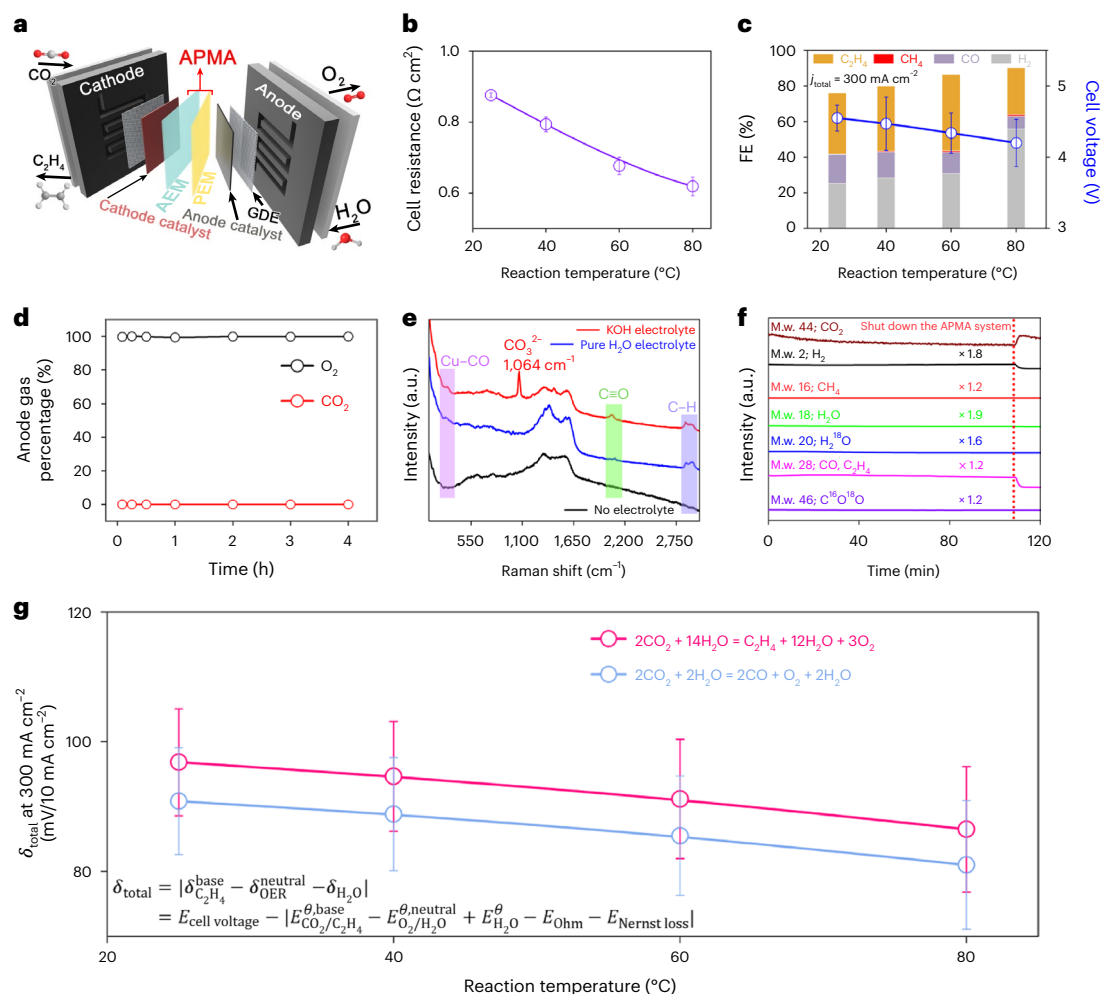


**Fig. 4 | Implementing the prototype of the pure-H<sub>2</sub>O-fed APMA system for ECO<sub>2</sub>R on SS-Cu.** **a**, A schematic of the APMA-MEA system architecture for ECO<sub>2</sub>R. **b**, The resistance of the system at different reaction temperatures. **c**, The FEs of gas products and corresponding cell voltages of the system at a total current density of 300 mA cm<sup>-2</sup> for different reaction temperatures. **d**, The anodic gas product analysis of the pure-H<sub>2</sub>O-fed APMA system at 60 °C with a total current density of 300 mA cm<sup>-2</sup>. Ti fibre felt sputtered with Pt (Pt/Ti) was used as the anode electrode, and the flow rate of the CO<sub>2</sub> inlet was 30 sccm.

**e**, In situ Raman spectra of ECO<sub>2</sub>R on SS-Cu in 0.1 M KOH, pure H<sub>2</sub>O and bare electrode after -20 min. **f**, The mass spectra of ECO<sub>2</sub>R using H<sub>2</sub><sup>18</sup>O as the analyte in the APMA system. **g**, The total overpotential of all the reactions at different reaction temperatures. Values are means, and error bars indicate the s.d. (*n* = 3 replicates), except for **g**, where the values are means and the error bars indicate the effect of the AEM's pH on the overpotential (setting the pH of the AEM in the range of 8–14).

the pure-H<sub>2</sub>O analyte, the Nernst equation can be simplified to equation (6) at room temperature<sup>36</sup> (Supplementary Note 5). The analyte pH is -7 owing to the use of pure H<sub>2</sub>O. We assume that the OH<sup>-</sup> concentration on the AEM surface was 1 M (that is, pH 14), at which the potential drop ( $E_{\text{Nernst loss}}$ ) of the pure-H<sub>2</sub>O-fed APMA-MEA cell was about 0.41 V. Therefore, without considering overpotentials ( $\delta_{\text{C}_2\text{H}_4}^{\text{base}}$ ,  $\delta_{\text{OER}}^{\text{neutral}}$  and  $\delta_{\text{H}_2\text{O}}$ ) or  $E_{\text{ohm}}$ , the theoretical cell voltage of our pure-H<sub>2</sub>O-fed APMA-MEA system used for ECO<sub>2</sub>R to C<sub>2</sub>H<sub>4</sub> needs to be more negative than -1.56 V at standard conditions. Additionally, when considering the key intermediate (CO) of C<sub>2</sub>H<sub>4</sub> formation ( $E_{\text{CO}_2/\text{CO}}^{\theta, \text{base}} = -0.93$  V), the theoretical cell voltage would be up to -1.74 V.

The above findings suggest that the operating voltage of the pure-H<sub>2</sub>O-fed APMA-MEA system needs to be lowered for effective energy conversion. In other words, the overpotentials of all the reactions, including ECO<sub>2</sub>R, the OER and water formation, must be minimized. Indeed, when we increased the reaction temperature of ECO<sub>2</sub>R on SS-Cu in the pure-H<sub>2</sub>O-fed APMA-MEA system from room temperature (-25 °C) to 80 °C (Fig. 4c), the cell voltage decreased from -4.55 to 4.20 V at 300 mA cm<sup>-2</sup>. Meanwhile, the cell resistance was reduced by -0.257 Ω cm<sup>2</sup> at 80 °C (Fig. 4b), meaning a voltage drop of -0.08 V.

However, the cell voltage drop of -0.35 V was much more than -0.08 V, indicating that increasing the reaction temperature mainly lowers the overpotentials. The optimal FEs for ECO<sub>2</sub>R were achieved at 60 °C, where the FEs for carbon gas products and H<sub>2</sub> were -55.67% (-12.03% for CO, -0.76% for CH<sub>4</sub> and -42.88% for C<sub>2</sub>H<sub>4</sub>) and -30.81% (Fig. 4c), respectively. However, when the reaction temperature was increased to 80 °C, the FE of H<sub>2</sub> was even over 50%, indicating that excessive temperature would suppress ECO<sub>2</sub>R and make the HER dominant. Thus, the following ECO<sub>2</sub>R tests were carried out at 60 °C.

Furthermore, the reaction kinetics of the pure-H<sub>2</sub>O-fed APMA-MEA system for ECO<sub>2</sub>R was quantified. The total overpotential ( $\delta_{\text{total}}$ ) at a given current density, including ECO<sub>2</sub>R, the OER and water formation, was assessed at different temperatures by using the Gibbs-Helmholtz and Nernst equations ( $\delta_{\text{total}}$  is defined in Supplementary Note 5). Owing to the lack of pH data for the commercial AEM, we assume the pH of AEM to be in the range of 8–14. Taking ECO<sub>2</sub>R to C<sub>2</sub>H<sub>4</sub> as an example without considering other products,  $\delta_{\text{total}}$  decreased with increase of the reaction temperature (Fig. 4g). At 300 mA cm<sup>-2</sup> and 60 °C, the total overpotential ( $\delta_{\text{total}}$ ) of the system was -91.17 mV/10 mA cm<sup>-2</sup>. Considering the key intermediate (CO),  $\delta_{\text{total}}$  was only -85.50 mV/10 mA cm<sup>-2</sup>

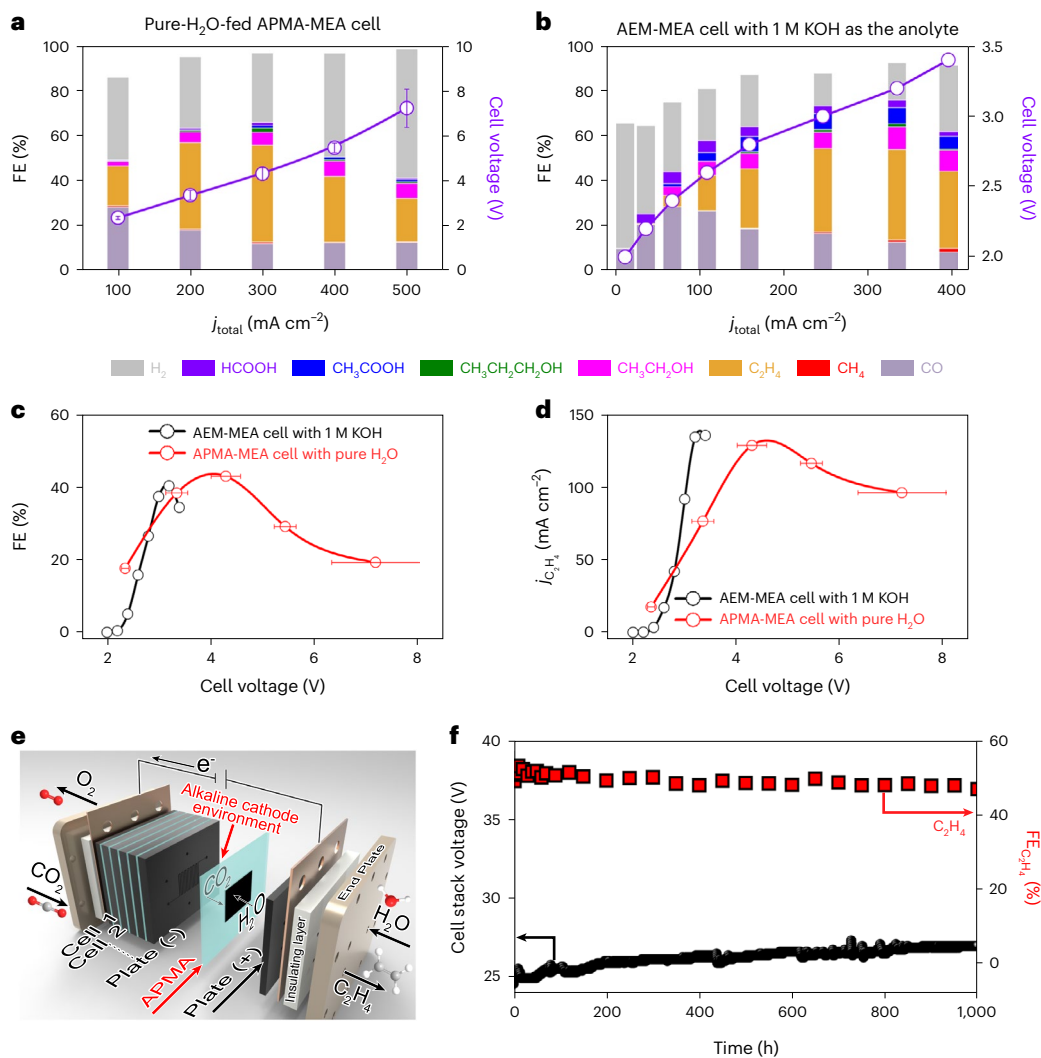


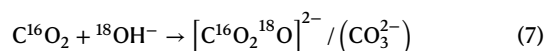
**Fig. 5 | The Overall ECO<sub>2</sub>R system performance of SS-Cu in the pure-H<sub>2</sub>O-fed APMA-MEA cell/cell stack. a**, The FEs towards ECO<sub>2</sub>R products under a range of applied current densities, and the corresponding cell voltages without *iR* compensation. **b**, The FEs towards ECO<sub>2</sub>R products under a range of applied cell voltages without *iR* compensation, and the corresponding total current density. **c,d**, Comparisons of the FEs (c) and partial current densities (d) towards C<sub>2</sub>H<sub>4</sub> in the pure-H<sub>2</sub>O-fed APMA-MEA and AEM-MEA systems with 1 M KOH as the anolyte. **e**, A schematic of the APMA-MEA cell stack containing six APMA-MEA cells for

the ECO<sub>2</sub>R reaction. **f**, The system stability performance of ECO<sub>2</sub>R to C<sub>2</sub>H<sub>4</sub> on SS-Cu in a pure-H<sub>2</sub>O-fed APMA-MEA cell stack containing six APMA-MEA cells at a constant current of 10 A. Each cathode electrode area was 30 cm<sup>2</sup>, and the reaction temperature was 60 °C. Pt/Ti was used as the anode electrode, and the flow rate of the CO<sub>2</sub> inlet was 30 sccm for the single cell or cell stack. AEM and PEM membranes were used as the electrogenerated OH<sup>-</sup> and H<sup>+</sup>/H<sub>3</sub>O<sup>+</sup> ion exchange membranes, respectively. Values are means, and error bars indicate the s.d. (*n* = 3 replicates).

at 300 mA cm<sup>-2</sup> (Fig. 4g). Despite using pure H<sub>2</sub>O as the anolyte, the APMA-MEA system still showed the potential for effective ECO<sub>2</sub>R to C<sub>2</sub>H<sub>4</sub>.

The pure-H<sub>2</sub>O-fed APMA-MEA system was further evaluated for its reliability in preventing carbonate formation/precipitation and anion crossover. Inductively coupled plasma mass spectroscopy showed that almost no cations were present in the pure H<sub>2</sub>O anolyte (Supplementary Fig. 41), except for Na<sup>+</sup> at part per billion level, originating from the water source. Then, we tested the anodic product compositions. As expected, only O<sub>2</sub> from the OER was present in the anode product without CO<sub>2</sub> loss (Fig. 4d and Supplementary Fig. 42). The anolyte did not contain the other neutral species (such as HCOOH and CH<sub>3</sub>COOH) from the cathode (Supplementary Fig. 42). Additionally, in situ Raman measurements directly showed that carbonate formation was effectively suppressed (the peak at -1,064 cm<sup>-1</sup>) on the SS-Cu GDE surface in our pure-H<sub>2</sub>O-fed APMA system, compared with that in the alkaline-electrolyte system (Fig. 4e and Supplementary Figs. 43–45).

Furthermore, to verify that the APMA system can suppress carbonate formation, rather than regenerating CO<sub>2</sub> by H<sup>+</sup> from the anolyte reacting with carbonate, we also performed an isotope labelling experiment (using H<sub>2</sub><sup>18</sup>O as the anolyte). If CO<sub>2</sub> can react with the electrogenerated <sup>18</sup>OH<sup>-</sup> into carbonate, one of the oxygens in the carbonate will be <sup>18</sup>O (equation (7)). Thus, the regenerated CO<sub>2</sub> from these carbonates can be labelled by <sup>18</sup>O. However, the intensity of C<sup>16</sup>O<sup>18</sup>O (CO<sub>2</sub>) barely changed during the entire process when the APMA system was running and after shutdown (Fig. 4f), indicating that CO<sub>2</sub> did not react with the electrogenerated <sup>18</sup>OH<sup>-</sup> into carbonate. Instead, trace amounts of C<sup>16</sup>O<sup>18</sup>O come from the initial reactant CO<sub>2</sub> because the C<sup>16</sup>O<sup>18</sup>O intensity did not change during or after ECO<sub>2</sub>R. These results suggest that, under forward bias, the pure-H<sub>2</sub>O-fed APMA-MEA system configuration can effectively prevent carbonate formation/precipitation and anion crossover.



We examined the  $\text{ECO}_2\text{R}$  product distribution of SS-Cu in the pure- $\text{H}_2\text{O}$ -fed APMA-MEA system at  $60^\circ\text{C}$ , under the galvanostatic mode (Fig. 5a). At  $300\text{ mA cm}^{-2}$ , the peak FE of  $\text{ECO}_2\text{R}$  products reached  $\sim 66\%$ , including a  $\sim 52\%$  FE towards  $\text{C}_2^+$  ( $\sim 43\%$  for  $\text{C}_2\text{H}_4$ ,  $\sim 6\%$  for  $\text{C}_2\text{H}_5\text{OH}$ ,  $\sim 2\%$  for  $\text{CH}_3\text{CH}_2\text{CH}_2\text{OH}$  and  $\sim 1\%$  for  $\text{CH}_3\text{COOH}$ ). The cell voltage was  $\sim 4.3\text{ V}$  without  $iR$  ( $i$ , current;  $R$ , resistance) compensation. Without counting the energy consumed by the reaction temperature, the pure- $\text{H}_2\text{O}$ -fed APMA-MEA system delivered a full-cell energy efficiency ( $\text{EE}_{\text{full cell}}$ ) of  $\sim 18.2\%$  for  $\text{ECO}_2\text{R}$ . The peak FEs and partial current densities of products in the pure- $\text{H}_2\text{O}$ -fed APMA-MEA system were comparable to those in an AEM-MEA cell with  $1\text{ M KOH}$  as the anolyte (Fig. 5a–d and Supplementary Fig. 46). Furthermore, the system carbon balance at  $300\text{ mA cm}^{-2}$  was also evaluated by using a previous method<sup>34,37,38</sup>. All the  $\text{ECO}_2\text{R}$  products were recovered to the  $\text{CO}_2$  (Supplementary Fig. 47). The sum of the  $\text{CO}_2$  flow rate ( $\sim 29.76\text{ sccm}$ ) including  $\text{CO}_2$  recovered as products and unreacted  $\text{CO}_2$  is close to the initial  $\text{CO}_2$  flow rate ( $30\text{ sccm}$ ). The slight discrepancy can be attributed to a small amount of product residue or leakage. The carbon balance evaluation suggests that our APMA-MEA system has virtually no  $\text{CO}_2$  loss.

### The practicality of the pure- $\text{H}_2\text{O}$ -fed APMA-MEA cell for $\text{ECO}_2\text{R}$

Motivated by the superior  $\text{ECO}_2\text{R}$  performance exhibited by SS-Cu in the pure- $\text{H}_2\text{O}$ -fed APMA-MEA system, we designed and customized a cell stack containing six MEA cells to evaluate the durability and practicality of the pure- $\text{H}_2\text{O}$ -fed APMA-MEA architecture (Fig. 5e and Supplementary Fig. 48). This scale-up operation and stability measurements of the APMA-MEA cell stack could pave the way for  $\text{ECO}_2\text{R}$  to  $\text{C}_2\text{H}_4$  towards industrial-scale operation. At a total current of  $10\text{ A}$ , six SS-Cu GDEs give an FE of  $\sim 50\%$  towards  $\text{C}_2\text{H}_4$  (Fig. 5f). The system remained stable for more than  $1,000\text{ h}$  with a full-cell-stack voltage between  $25$  and  $27\text{ V}$  without  $iR$  compensation (a cell voltage of  $\sim 4.4\text{ V}$  for each set of MEA cells; Supplementary Fig. 49). In stark contrast, the system stability of  $\text{ECO}_2\text{R}$  on SS-Cu in an AEM-MEA cell with  $1\text{ M KOH}$  as the anolyte was less than  $4\text{ h}$ , with severe electrolyte and  $\text{CO}_2$  losses (Supplementary Fig. 50). Suppressing/preventing carbonate formation/precipitation using the pure- $\text{H}_2\text{O}$ -fed APMA system certainly boosted the system's durability, but the strong mechanical strength of APMA itself and the excellent water permeability of the commercial AEM and PEM (Sustainion X37-50 and Nafion 117) of the APMA were also conducive to improving the system stability at a non-extreme current density. The  $\text{CO}_2$ -to- $\text{C}_2\text{H}_4$  conversion in this alkali-cation-free six-APMA-MEA-cell stack was up to  $\sim 39\%$ . After  $1,000\text{ h}$  of operation, no GDE flooding was observed, which could be attributed to the increased reaction temperature ( $60^\circ\text{C}$ ) allowing  $\text{H}_2\text{O}$  accumulated in the GDEs to be discharged quickly along with the steam.

In this pure- $\text{H}_2\text{O}$ -fed APMA-MEA stack system, we also developed an integrated circuit based on an Arduino development board to monitor the  $\text{ECO}_2\text{R}$  process (Supplementary Fig. 49, inset). Accordingly, each cell showed identical voltage throughout the  $1,000\text{ h}$  measurement, except for some fluctuations during the first  $100\text{ h}$  (Supplementary Fig. 49), demonstrating the potential of the APMA-MEA stack for highly stable  $\text{ECO}_2\text{R}$  to  $\text{C}_2\text{H}_4$ , as demanded for industrial operation. The overall system performance of  $\text{ECO}_2\text{R}$  to  $\text{C}_2\text{H}_4$  on SS-Cu in our pure- $\text{H}_2\text{O}$ -fed APMA-MEA system is highly competitive with previous reports (Supplementary Fig. 2 and Supplementary Table 1). The overall system performance improvements of  $\text{ECO}_2\text{R}$  to  $\text{C}_2\text{H}_4$  in the pure- $\text{H}_2\text{O}$ -fed APMA-MEA system can be attributed to the combination of the APMA electrolysis architecture and the superior catalytic activity of SS-Cu.

In situ X-ray diffraction (XRD) measurements show that the crystal structure of SS-Cu is stable during  $\text{ECO}_2\text{R}$  at different cell voltages (Supplementary Figs. 51–53). Furthermore, annular bright-field STEM (ABF-STEM), TEM and HRTEM images show that the SS-Cu catalyst retained its structural integrity throughout the long  $\text{ECO}_2\text{R}$  operation (Supplementary Fig. 54). This can be judged from the presence

of atomically resolved stacking faults and grain boundaries (twin boundaries) in the HAADF-STEM images before and after prolonged  $\text{ECO}_2\text{R}$  (Supplementary Fig. 54).

### Investigation of $\text{C}_2\text{H}_4$ formation

The key intermediates of C–C coupling for  $\text{C}_2\text{H}_4$  formation on SS-Cu were studied by in situ Raman spectroscopy, electrocatalytic CO reduction experiments and density functional theory (DFT) calculations (see Supplementary Note 6 and Supplementary Figs. 55–59 for details). In situ Raman measurements revealed the presence of the intermediate  $^*\text{CO}$  and C–H bond, while the ECOR experiments excluded  $^*\text{CO}$  dimerization for  $\text{C}_2\text{H}_4$  formation. By comparing the reaction energy of possible reaction intermediates (such as  $^*\text{CHO}$  dimerization,  $^*\text{CO} + ^*\text{COH}$ ), the favourable C–C coupling of  $\text{C}_2\text{H}_4$  formation on SS-Cu might be that  $^*\text{CO}$  and  $^*\text{CHO}$  couple to  $^*\text{COCHO}$  owing to a lower reaction energy. The mechanism is similar to the mainstream  $\text{ECO}_2\text{R}$  to  $\text{C}_2\text{H}_4$  mechanism reported previously<sup>8,33</sup>, which means that the highly efficient performance cannot be attributed to a newly found reaction pathway, but rather to the successful regulation of ion and mass diffusion and the suppression of side reactions in the APMA-MEA system.

### Conclusions

We demonstrate that the pure- $\text{H}_2\text{O}$ -fed (alkali-cation-free) APMA-MEA system can effectively suppress/prevent carbonate formation/precipitation and anion crossover during  $\text{ECO}_2\text{R}$  while circumventing the burdensome HER as well as  $\text{CO}_2$  and electrolyte losses. The simplicity of the system design improves the overall system performance for  $\text{ECO}_2\text{R}$  by maintaining an alkaline cathode environment without supplying alkali cations. The extensive experiments reveal that the pure- $\text{H}_2\text{O}$ -fed APMA system can effectively suppress/prevent carbonate formation/precipitation rather than regenerate  $\text{CO}_2$  from carbonate. At an industrial-level current, the overall system stability of scaled-up  $\text{ECO}_2\text{R}$  to  $\text{C}_2\text{H}_4$  on SS-Cu is significantly enhanced in the pure- $\text{H}_2\text{O}$ -fed APMA-MEA cell stack. However, although our system showed competitive system performance for  $\text{ECO}_2\text{R}$  to  $\text{C}_2\text{H}_4$ , further improving the product selectivity and lowering the operation voltage are still required for efficient energy conversion.

### Methods

#### Chemicals

Deuterium oxide ( $\text{D}_2\text{O}$ , 99.9 at. % D; 151882), 3-(trimethylsilyl) propionic-2,2,3,3- $\text{d}_4$  acid sodium salt (TSP,  $\geq 98.0\%$  (NMR); 269913), Nafion solution (5 wt.%; 274704), polytetrafluoroethylene preparation (60% solution in  $\text{H}_2\text{O}$ ; 665800), oleylamine (70%; 07805), copper(I) chloride ( $\text{CuCl}$ , 97%; 212946),  $n$ -hexane ( $\text{C}_6\text{H}_{14}$ , 99%; HX0293), octadecylamine ( $\geq 99\%$ ; 305391), trioctylphosphine (90%; 117854), squalane (96%; 234311), potassium hydroxide ( $\text{KOH}$ , 99.99%; 306568), phosphoric acid ( $\text{H}_3\text{PO}_4$ , 85%; 345245), potassium nitrate ( $\text{KNO}_3$ , 99.0%; 221295), lead(II) nitrate ( $\text{Pb}(\text{NO}_3)_2$ ,  $\geq 99\%$ ; 228621), potassium iodide ( $\text{KI}$ , 99%; 221945), water- $^{18}\text{O}$  ( $^{18}\text{O}$   $\text{H}_2\text{O}$ , 10 at. %  $^{18}\text{O}$ ; 332089) and potassium chloride ( $\text{KCl}$ , 99.0–100.5%; P3911) were purchased from Sigma Aldrich. Potassium hydroxide ( $\text{KOH}$ ,  $\geq 85.0\%$ ), nickel foam (2 mm thickness, 99.9%) and titanium fibre felt (0.25 mm thickness, 99.9%) were purchased from Sinopharm Chemical Reagent Co., Ltd. (China). Nitric acid ( $\text{HNO}_3$ , pH  $\sim 1.0$ , 70%; A200) and isopropanol ( $\text{C}_3\text{H}_8\text{O}$ , IPA,  $\geq 99.5\%$ ; 3776) were purchased from Fisher Scientific. The AEM (Fumasep FAA-3-PK-75), gas diffusion layer (carbon paper, GDE; Sigracet 39 BB) and Nafion 117 membrane (591239) were purchased from FuelCellStore. The alkaline ionomer solution (5% in ethanol, Sustainion XA-9) and AEM (Sustainion X37-50) were purchased from Dioxide Materials.

#### Material and electrode preparation

In a typical synthesis,  $0.05\text{ g}$  of  $\text{CuCl}$  and  $0.1\text{ g}$  of octadecylamine were dissolved in  $1\text{ ml}$  of squalane at  $80^\circ\text{C}$  under Ar atmosphere and kept at this temperature for  $0.5\text{ h}$  to form Cu-based stock solution.



Next, 10 ml of oleylamine and 0.5 ml of trioctylphosphine were added to a flask and heated to 200 °C under Ar atmosphere with intense magnetic agitation. Then, the Cu-based stock solution was quickly injected into the about 200 °C oleylamine solution and kept at this temperature for 5 h. After natural cooling, the resulting sample was collected by centrifugation and washed several times with *n*-hexane. Finally, the sample was blow-dried with Ar gas at room temperature. The sample was denoted as SS-Cu.

The SS-Cu samples were annealed at various temperatures (250, 350 and 450 °C; Cu-250, Cu-350 and Cu-450) in a tube furnace for 2 h under a mixed gas (H<sub>2</sub>/Ar: 5 v/v%; 200 sccm) to prevent oxidization. In addition, the oxide-derived Cu was prepared by directly calcining SS-Cu at 450 °C in air for 2 h.

The flow cell and MEA cell measurements under the alkaline condition were carried out as follows: Cathode GDEs were prepared on conventional carbon paper. The catalyst was dispersed in a mixed solution containing H<sub>2</sub>O and isopropyl alcohol (IPA) (1:4 v/v), and some alkaline ionomer solution (5 wt.% versus catalyst, Sustainion XA-9) by sonication for 1 h to form a 1 mg ml<sup>-1</sup> catalyst ink. GDEs were fabricated by spraying the ink onto the carbon paper with a microporous carbon gas diffusion layer with a loading of -1 mg cm<sup>-2</sup>, followed by drying at 120 °C in vacuum for 1 h before use (SS-Cu GDE). The anode electrode was a mixture of IrO<sub>x</sub> and RuO<sub>x</sub>-supported carbon paper.

The flow cell and MEA cell measurements under the acidic condition were carried out as follows: The alkaline ionomer was replaced with Nafion solution. Polymethylmethacrylate containing polytetrafluoroethylene solution was sprayed on the SS-Cu GDE as the cathode GDE (SS-Cu/polymethylmethacrylate). The mixture of Pt-supported Ti fibre felt (Pt/Ti) was used as the anode electrode. Pt was sputtered on the Ti fibre felt using a pure Pt target in Ar environment (5 × 10<sup>-3</sup> Torr) in a magnetron sputtering system.

For MEA measurements under pure H<sub>2</sub>O, the SS-Cu GDE and Pt/Ti GDE were directly used as the cathode and anode electrodes, respectively.

### Electrocatalytic CO<sub>2</sub>/CO reduction

Electrochemical tests in the flow and MEA cells were performed using an electrochemical workstation (CHI 660E) connected to a current booster (CHI 680C), except for the MEA cell stack. A mass flow controller (Alicat Scientific MC) was used to control the CO<sub>2</sub> flow rate. The flow rate of the electrolyte stream was 5 ml min<sup>-1</sup>, controlled by a peristaltic pump unless otherwise noted. The cathode area in the flow cell and MEA was 1 cm × 1 cm unless otherwise noted. All ECO<sub>2</sub>R measurements were carried out at room temperature unless otherwise noted. For all flow cell measurements, Hg/Hg<sub>2</sub>Cl<sub>2</sub> (saturated calomel electrode, saturated KCl) was used as the reference electrode, and all cathode potentials (versus Hg/Hg<sub>2</sub>Cl<sub>2</sub>) were converted to the RHE scale using the equation

$$E_{(\text{RHE})} = E_{(\text{Hg}/\text{Hg}_2\text{Cl}_2)} + 0.241 + 0.0591 \times \text{pH} + iR$$

where *R* is the resistance between the cathode and reference electrodes measured by electrochemical impedance spectroscopy in the frequency range from 10<sup>5</sup> Hz to 0.01 Hz at open circuit potential. For all the MEA measurements, the full-cell voltages are directly presented without *iR* compensation.

Under the alkaline condition, for the flow cell measurements, 1 M KOH was used as the electrolyte, and the AEM (Fumasep FAA-3-PK-75) was used to separate the catholyte and anolyte compartments. CO<sub>2</sub>/CO was supplied to the cathode at a flow rate of 30 sccm. For ECO<sub>2</sub>R in an MEA cell with the alkaline condition, 1 M KOH was used as the anolyte, and the cathode and anode GDEs were separated by an AEM (Sustainion X37-50).

Under the acidic condition, for the flow cell measurements, 1 M H<sub>3</sub>PO<sub>4</sub> with 3 M KCl/KI was used as the catholyte, and 1 M H<sub>3</sub>PO<sub>4</sub> was

used as the anolyte. The cathode and anode chambers were separated by Nafion 117. For MEA measurements, 1 M H<sub>3</sub>PO<sub>4</sub> with 3 M KNO<sub>3</sub> was used as the anolyte. CO<sub>2</sub> was supplied to the cathode at a flow rate of 30 sccm.

For scale-up APMA-MEA stack measurements, an integrated circuit based on an Arduino development board (UNO R3, A000066) was used as an aided monitoring system connected with the CoolTerm serial port terminal application tool. All ECO<sub>2</sub>R measurements in the APMA-MEA stack were carried out by using a customized Varied d.c. power supply (1,000 W). The flow rates of the anolyte and CO<sub>2</sub> were 15 ml min<sup>-1</sup> and 30 sccm, respectively. The reaction temperature was 60 °C. For the APMA system, before assembly, the AEM was cleaned with pure H<sub>2</sub>O to eliminate other ions since AEM was immersed in 1 M KOH beforehand. The commercial PEM was soaked in ~3% hydrogen peroxide for 1 h at 80 °C, deionized water for 1 h at 80 °C and 0.5 M H<sub>2</sub>SO<sub>4</sub> for another 1 h at 80 °C. The resulting PEM was cleaned with pure H<sub>2</sub>O and preserved in deionized water at room temperature.

### Product analysis

For the electrocatalytic CO<sub>2</sub> and CO reduction, the gas and liquid products were quantified by gas chromatography (GC, GC-2030; Shimadzu) and nuclear magnetic resonance (NMR, ECZ500R, 500 MHz; JEOL) spectroscopy. The GC device was equipped with two thermal conductivity detectors for H<sub>2</sub>, O<sub>2</sub>, N<sub>2</sub>, He, CO and CO<sub>2</sub> signals and a flame ionization detector for CH<sub>4</sub>, C<sub>2</sub>H<sub>4</sub> and C<sub>2</sub>H<sub>6</sub> signals. The GC was carried out using packed columns of two Porapak-N, a Molecular sieve-13X, a Molecular sieve-5A, a Porapak-Q and an HP-PLOT AL/S column, employing He (99.999%) and N<sub>2</sub> (99.999%) as the carrier gases. To calibrate the CO<sub>2</sub> flow rate at the outlet of the cell (*f*<sub>CO<sub>2</sub></sub>), He used as the internal standard was fed at 10 sccm and mixed with the outlet gas stream of the cell before injecting for GC<sup>34</sup>. The FEs of gas products were calculated by using the equation

$$\text{FE}(\%) = N_x \times F \times m_x \times \frac{f_{\text{CO}_2}}{j_{\text{total}}} \times 100\%,$$

where *N<sub>x</sub>* is the number of electrons transferred for product *x*, *F* is the Faradaic constant, *m<sub>x</sub>* is the molar fraction of product *x* determined by GC, *f*<sub>CO<sub>2</sub></sub> is the molar flow rate of the CO<sub>2</sub> and *j*<sub>total</sub> is the total current density.

The liquid products were analysed by 500 MHz <sup>1</sup>H NMR spectroscopy (ECZ500R; JEOL) with water suppression. TSP and D<sub>2</sub>O were used as the reference standard and lock solvent, respectively. The FEs of liquid products were calculated by using the equation

$$\text{FE}(\%) = N_x \times F \times \frac{C_x \times V_x}{Q_{\text{total}}} \times 100\%,$$

where *N<sub>x</sub>* is the number of electrons transferred for liquid product *x*, *F* is the Faradaic constant, *C<sub>x</sub>* is the concentration of liquid product *x* determined by <sup>1</sup>H NMR, *V<sub>x</sub>* is the volume of the electrolyte and *Q*<sub>total</sub> is the total charge.

The half-cell and full-cell energy efficiencies (EE<sub>half cell</sub> and EE<sub>full cell</sub>) were calculated using the following equations (taking the OER as an example of the anode reaction and assuming it occurs with an overpotential of 0 V, *E*<sup>o</sup><sub>OER</sub> = 1.23 V versus RHE):

$$\begin{aligned} \text{EE}_{\text{half cell}}(\%) &= \frac{(E_{\text{OER}}^{\text{O}} - E_x^{\text{O}}) \times \text{FE}_x}{E_{\text{OER}}^{\text{O}} - E_c} \times 100\% \\ &= \frac{(1.23 - E_x^{\text{O}}) \times \text{FE}_x}{1.23 - E_c} \times 100\%, \end{aligned}$$

$$\begin{aligned} \text{EE}_{\text{full cell}}(\%) &= (E_{\text{OER}}^{\text{O}} - E_x^{\text{O}}) / E_{\text{full cell}} \times \text{FE}_x \times 100\% \\ &= \frac{1.23 - E_x^{\text{O}}}{E_{\text{full cell}}} \times \text{FE}_x \times 100\%, \end{aligned}$$



where  $E_{\text{OER}}^{\theta}$  and  $E_x^{\theta}$  are the thermodynamic potentials (versus RHE) for OER and the  $\text{CO}_2\text{R}$  to product  $x$ , respectively,  $FE_x$  is the FE of product  $x$ ,  $E_c$  is the potential applied at the cathode and  $E_{\text{full cell}}$  is the cell voltage of the MEA system.

The  $\text{CO}_2$  conversion was calculated using the equations

$$f_x = \frac{Q_{\text{total}} \times FE_x}{F \times N_x \times t \times A}$$

$$\begin{aligned} \text{CO}_2 \text{ conversion (\%)} = & (f_{\text{CO}} + f_{\text{HCOO}^-} + f_{\text{CH}_4} + 2f_{\text{C}_2\text{H}_4} \\ & + 2f_{\text{C}_2\text{H}_5\text{OH}} + 2f_{\text{CH}_3\text{COO}^-} + 3f_{1-\text{C}_3\text{H}_7\text{OH}}) \times \frac{A}{f_{\text{CO}_2}} \times 100\%, \end{aligned}$$

where  $f_x$  is the molar rate of formation of product  $x$ ,  $t$  is the electrolysis reaction time and  $A$  is the geometric area of the electrode.

### In situ electrochemical Raman measurements

In situ Raman measurements were carried out by using a customized spectro-electrochemical flow cell fabricated with a sapphire window ( $0.15 \pm 0.02$  mm) in front of the cathode GDE. Ni felt was used as a counterelectrode. The overall system was operated in a two-electrode set-up. The electrolyte (0.1 M KOH) was pumped into a sapphire window at a constant flow rate of  $5 \text{ ml min}^{-1}$  by using a peristaltic pump over the cathode GDE, and the thickness of the electrolyte level on the cathode surface was 1.5 mm.  $\text{CO}_2$  was supplied to the back of the cathode GDE through a serpentine flow channel to guide the  $\text{CO}_2$  at a flow rate of 30 sccm, controlled by a mass flow controller (Alicat Scientific MC). Raman spectra were collected using an accumulation time of 4 s and an accumulation number of ten times using a WITEC confocal Raman microscope with a  $50\times$  objective and a 633 nm laser. The cell voltage was applied in potentiostatic mode and recorded without  $iR$  compensation.

### In situ electrochemical XRD measurements

The customized spectro-electrochemical flow cell was employed to perform in situ XRD measurements in a two-electrode set-up. Ni felt was used as a counterelectrode, 0.1 M KOH was used as the electrolyte and  $\text{CO}_2$  (30 sccm) was supplied to the back of the cathode GDE. The in situ XRD patterns were collected on an X-ray diffractometer (Rigaku SmartLab 9 kW, Advance) using Cu K $\alpha$  radiation ( $\lambda = 1.5418 \text{ \AA}$ ) at 45 kV and 200 mA. The single test time was about ~8 min in the  $2\theta$  range of  $30\text{--}85^\circ$ . The cell voltage was applied in potentiostatic mode and recorded without  $iR$  compensation.

### In situ heating TEM measurements

In situ heating TEM measurements were performed on a JEOL JEM-2100F at 200 kV with a Fusion Select holder (Protochips) and a holey carbon-coated micro-electromechanical system E-chip (E-FHBC-10, Protochips).

### Pb underpotential deposition measurements

The relative populations of the exposed facets of Cu were probed using Pb underpotential deposition measurements conducted in a three-electrode single-compartment cell. A graphite carbon rod and Ag/AgCl (3 M KCl) were used as the counterelectrode and reference electrode, respectively. An L-type glassy-carbon electrode loaded with the sample with a diameter of 3 mm was employed as the working electrode.  $\text{N}_2$ -purged 0.1 M  $\text{KNO}_3$  with 1 mM  $\text{Pb}(\text{NO}_3)_2$  was added with  $\text{HNO}_3$  to adjust the pH to 1, used as the electrolyte. Cyclic voltammetry at a sweep rate of  $100 \text{ mV s}^{-1}$  was used for measurements.

### Temperature-programmed desorption measurements

Temperature-programmed desorption measurements of  $\text{CO}_2$  on samples were conducted by using an adsorption/desorption system. In a typical experiment,  $1 \text{ cm}^2$  GDE with a catalyst load of  $\sim 1 \text{ mg cm}^{-2}$

was ground into powder that was then placed in a U-shaped quartz microreactor. Next, the outlet of the U-shaped quartz microreactor was connected to the GC device (GC-2014, Shimadzu) with a thermal conductivity detector. Afterwards,  $\text{CO}_2$  (40 sccm) was injected into the U-shaped quartz microreactor and kept flowing for 60 min, followed by flushing the sample using a He stream (40 sccm) until obtaining a stable baseline in GC. Temperature-programmed desorption measurements were then conducted from room temperature to  $800/500 \text{ }^\circ\text{C}$  at a ramp rate of  $10 \text{ }^\circ\text{C min}^{-1}$ , using GC to detect the  $\text{CO}_2$  desorbed from the sample surface.

### DFT calculations

All DFT calculations were performed using the Vienna Ab initio Simulation Program. The generalized gradient approximation with the Perdew–Burke–Ernzerhof<sup>51</sup> exchange–correlation functional was adopted to describe the electronic exchange and correlation interactions with a cut-off energy of 500 eV. The energy convergence criteria were set to  $10^{-5}$  eV for self-consistent calculations, and the lattice parameters were optimized until the convergence tolerance of the force on each atom was smaller than 0.05 eV. A  $4 \times 4 \times 1$  Monkhorst–Pack  $k$ -point mesh was used for the Brillouin zone integration.

For perfect Cu, the copper crystal structure was optimized with a lattice constant of  $a = 3.636 \text{ \AA}$ . For Cu-SF, the unit cell was expanded by a factor of 1.1 and then fully relaxed until convergence. The lattice constant was determined to be  $4.000 \text{ \AA}$ . Six-layer  $p(4 \times 4)$  supercells of Cu(111) facet were used, with the lower three layers fixed. For all slab models, the vacuum thickness in a direction perpendicular to the plane of the catalyst was at least  $15 \text{ \AA}$  to avoid attractions from adjacent periodic mirror images. At all intermediate states, two water molecules are added near the slab surface to consider the effect of solvation.

The Gibbs free energy ( $\Delta G$ ) of the reaction intermediates was defined as

$$\Delta G = \Delta E + \Delta \text{ZPE} - T\Delta S,$$

where  $\Delta E$  is the total energy difference,  $\Delta \text{ZPE}$  is the difference of the zero-point energy and  $T\Delta S$  is the difference of entropy. Note that  $E(\text{H})$  is half of the  $\text{H}_2(\text{g})$  energy under 1.013 bar at 298.15 K,  $E(\text{H}_2\text{O})$  is the energy of  $\text{H}_2\text{O}(\text{g})$  under 0.035 bar at 298.15 K and  $E(\text{OH}) = E(\text{H}_2\text{O}) - E(\text{H})$ . The zero-point energy and entropy were corrected by calculating the vibrational frequencies through density functional perturbation theory at 298.15 K.

### Characterization

TEM images were collected on a JEOL JEM-2100F at 200 kV. Aberration-corrected HAADF-STEM images were collected on a TFS Spectra 300 at 300 kV. GPA analysis on atomic-resolution images was performed using Digital Micrograph software to derive the lattice strain. Only strain perpendicular to the stacking faults and twin boundaries was measured, using the lattice far from these defects as a reference (zero strain). Scanning electron microscopy images were taken on a field-emission Tescan MAIA3. The XRD patterns were recorded on a Rigaku SmartLab 9 kW Advance diffractometer with Cu K $\alpha$  radiation ( $\lambda = 1.5418 \text{ \AA}$ ). XPS spectra were collected on a Thermo Scientific Nexsa X-ray photoelectron spectroscopy using Al K $\alpha$  radiation with C 1s (284.6 eV) as a reference. ICP-MS spectra were collected on an Agilent 7900. The hard X-ray absorption spectroscopy measurements were conducted at beamline BL01C of the Synchrotron Radiation Research Center in Hsinchu, Taiwan.

### Data availability

The authors declare that all data supporting the findings of this study are available within the paper and Supplementary Information files. Source data are provided with this paper.

## References

1. De Luna, P. et al. What would it take for renewably powered electrosynthesis to displace petrochemical processes? *Science* **364**, eaav3506 (2019).
2. Wakerley, D. et al. Gas diffusion electrodes, reactor designs and key metrics of low-temperature CO<sub>2</sub> electrolyzers. *Nat. Energy* **7**, 130–143 (2022).
3. Mariano, R. G., McKelvey, K., White, H. S. & Kanan, M. W. Selective increase in CO<sub>2</sub> electroreduction activity at grain-boundary surface terminations. *Science* **358**, 1187–1192 (2017).
4. Xia, C. et al. Continuous production of pure liquid fuel solutions via electrocatalytic CO<sub>2</sub> reduction using solid-electrolyte devices. *Nat. Energy* **4**, 776–785 (2019).
5. Zhong, M. et al. Accelerated discovery of CO<sub>2</sub> electrocatalysts using active machine learning. *Nature* **581**, 178–183 (2020).
6. García de Arquer, F. P. et al. CO<sub>2</sub> electrolysis to multicarbon products at activities greater than 1 A cm<sup>-2</sup>. *Science* **367**, 661–666 (2020).
7. Morales-Guio, C. G. et al. Improved CO<sub>2</sub> reduction activity towards C<sub>2+</sub> alcohols on a tandem gold on copper electrocatalyst. *Nat. Catal.* **1**, 764–771 (2018).
8. She, X. J., Wang, Y. F., Xu, H., Tsang, S. C. E. & Lau, S. P. Challenges and opportunities of electrocatalytic CO<sub>2</sub> reduction to chemicals and fuels. *Angew. Chem. Int. Ed.* **134**, e202211396 (2022).
9. Monteiro, M. C. O. et al. Absence of CO<sub>2</sub> electroreduction on copper, gold and silver electrodes without metal cations in solution. *Nat. Catal.* **4**, 654–662 (2021).
10. Zhang, F. & Co, A. C. Direct evidence of local pH change and the role of alkali cation during CO<sub>2</sub> electroreduction in aqueous media. *Angew. Chem. Int. Ed.* **58**, 1674–1681 (2019).
11. Huang, J. E. et al. CO<sub>2</sub> electrolysis to multicarbon products in strong acid. *Science* **372**, 1074–1078 (2021).
12. Yang, K. L. et al. Cation-driven increases of CO<sub>2</sub> utilization in a bipolar membrane electrode assembly for CO<sub>2</sub> electrolysis. *ACS Energy Lett.* **6**, 4291–4298 (2021).
13. Endrődi, B. et al. Operando cathode activation with alkali metal cations for high current density operation of water-fed zero-gap carbon dioxide electrolyzers. *Nat. Energy* **6**, 439–448 (2021).
14. Liu, Z. C., Yang, H. Z., Kutz, R. & Masel, R. I. CO<sub>2</sub> electrolysis to CO and O<sub>2</sub> at high selectivity, stability and efficiency using sustainion membranes. *J. Electrochem. Soc.* **165**, J3371 (2018).
15. Rabinowitz, J. A. & Kanan, M. W. The future of low-temperature carbon dioxide electrolysis depends on solving one basic problem. *Nat. Commun.* **11**, 5231 (2020).
16. Ozden, A. et al. Cascade CO<sub>2</sub> electroreduction enables efficient carbonate-free production of ethylene. *Joule* **5**, 706–719 (2021).
17. Siritanaratkul, B. et al. Zero-gap bipolar membrane electrolyzer for carbon dioxide reduction using acid-tolerant molecular electrocatalysts. *J. Am. Chem. Soc.* **144**, 7551–7556 (2022).
18. Gu, J. et al. Modulating electric field distribution by alkali cations for CO<sub>2</sub> electroreduction in strongly acidic medium. *Nat. Catal.* **5**, 268–276 (2022).
19. O'Brien, C. P. et al. Single pass CO<sub>2</sub> conversion exceeding 85% in the electrosynthesis of multicarbon products via local CO<sub>2</sub> regeneration. *ACS Energy Lett.* **6**, 2952–2959 (2021).
20. Ovalle, V. J., Hsu, Y. S., Agrawal, N., Janik, M. J. & Waagele, M. M. Correlating hydration free energy and specific adsorption of alkali metal cations during CO<sub>2</sub> electroreduction on Au. *Nat. Catal.* **5**, 624–632 (2022).
21. Pribyl-Kranewitter, B., Beard, A., Schuler, T., Diklić, N. & Schmidt, T. J. Investigation and optimisation of operating conditions for low-temperature CO<sub>2</sub> reduction to CO in a forward-bias bipolar-membrane electrolyser. *J. Electrochem. Soc.* **168**, 043506 (2021).
22. Pătru, A., Binninger, T., Pribyl, B. & Schmidt, T. J. Design principles of bipolar electrochemical co-electrolysis cells for efficient reduction of carbon dioxide from gas phase at low temperature. *J. Electrochem. Soc.* **166**, F34–F43 (2019).
23. Pärnamäe, R. et al. Bipolar membranes: a review on principles, latest developments, and applications. *J. Membr. Sci.* **617**, 118538 (2021).
24. Oener, S. Z., Foster, M. J. & Boettcher, S. W. Accelerating water dissociation in bipolar membranes and for electrocatalysis. *Science* **369**, 1099–1103 (2020).
25. Chen, L. H. K., Xu, Q. C., Oener, S. Z., Fabrizio, K. & Boettcher, S. W. Design principles for water dissociation catalysts in high-performance bipolar membranes. *Nat. Commun.* **13**, 3846 (2022).
26. Xie, K. et al. Bipolar membrane electrolyzers enable high single-pass CO<sub>2</sub> electroreduction to multicarbon products. *Nat. Commun.* **13**, 3609 (2022).
27. Li, W. Z. et al. Bifunctional ionomers for efficient co-electrolysis of CO<sub>2</sub> and pure water towards ethylene production at industrial-scale current densities. *Nat. Energy* **7**, 835–843 (2022).
28. Feng, X. F., Jiang, K. L., Fan, S. S. & Kanan, M. W. Grain-boundary-dependent CO<sub>2</sub> electroreduction activity. *J. Am. Chem. Soc.* **137**, 4606–4609 (2015).
29. Mariano, R. G. et al. Microstructural origin of locally enhanced CO<sub>2</sub> electroreduction activity on gold. *Nat. Mater.* **20**, 1000–1006 (2021).
30. Feng, X. F., Jiang, K. L., Fan, S. S. & Kanan, M. W. A direct grain-boundary-activity correlation for CO electroreduction on Cu nanoparticles. *ACS Cent. Sci.* **2**, 169–174 (2016).
31. Huang, W. X. et al. Steam-created grain boundaries for methane C–H activation in palladium catalysts. *Science* **373**, 1518–1523 (2021).
32. Yin, Z. L. et al. An alkaline polymer electrolyte CO<sub>2</sub> electrolyzer operated with pure water. *Energy Environ. Sci.* **12**, 2455–2462 (2019).
33. Nitopi, S. et al. Progress and perspectives of electrochemical CO<sub>2</sub> reduction on copper in aqueous electrolyte. *Chem. Rev.* **119**, 7610–7672 (2019).
34. She, X. J. et al. Tandem electrodes for carbon dioxide reduction into C<sub>2+</sub> products at simultaneously high production efficiency and rate. *Cell Rep. Phys. Sci.* **1**, 100051 (2020).
35. Chen, C. B. et al. Cu-Ag tandem catalysts for high-rate CO<sub>2</sub> electrolysis toward multicarbons. *Joule* **4**, 1688–1699 (2020).
36. Ramdin, M. et al. High pressure electrochemical reduction of CO<sub>2</sub> to formic acid/formate: a comparison between bipolar membranes and cation exchange membranes. *Ind. Eng. Chem. Res.* **58**, 1834–1847 (2019).
37. Kim, J. Y. T. et al. Recovering carbon losses in CO<sub>2</sub> electrolysis using a solid electrolyte reactor. *Nat. Catal.* **5**, 288–299 (2022).
38. Ma, M. et al. Insights into the carbon balance for CO<sub>2</sub> electroreduction on Cu using gas diffusion electrode reactor designs. *Energy Environ. Sci.* **13**, 977–985 (2020).

## Acknowledgements

We thank the National Synchrotron Radiation Center, Hsinchu, Taiwan, for the use of beamline BL01C. We thank Arduino for open-source hardware and software. This work was financially supported by the Research Grants Council of Hong Kong (C5029-18E) and Hong Kong Polytechnic University (1-CD7U, 1-YXA0 and Q-CDAK) and the National Natural Science Foundation of China (22108109 and 22178152).

## Author contributions

S.P.L. supervised the project. X.S. and S.P.L. conceived the idea, designed all the electrolysis cells and performed catalyst synthesis, characterization, catalytic tests and data analysis. X.S. and L.Z. carried out all the electrochemical experiments. L.Z. carried out the DFT simulations. Y.W. contributed to the data analysis. P.X., T.-S.W. and M.M.-J.L. performed the coordination number and strain data

analyses. M.C.W. and X.S. designed the circuit based on Arduino and wrote the program. Y.Z., Z.X. and X.G. performed the high-resolution scanning transmission electron microscopy measurements. H.L. and H.X. assisted with catalyst synthesis. X.S. wrote the paper. S.P.L., Y.W. and S.C.E.T. revised the paper. All authors discussed the results and assisted with the paper preparation.

### Competing interests

S.P.L. and X.S. have filed a US patent (application no. 17/806102) regarding the catalyst and the MEA architecture. The other authors declare no competing interests.

### Additional information

**Supplementary information** The online version contains supplementary material available at <https://doi.org/10.1038/s41560-023-01415-4>.

**Correspondence and requests for materials** should be addressed to Hui Xu, Ye Zhu, Shik Chi Edman Tsang or Shu Ping Lau.

**Peer review information** *Nature Energy* thanks Yan Jiao and the other, anonymous, reviewer(s) for their contribution to the peer review of this work.

**Reprints and permissions information** is available at [www.nature.com/reprints](http://www.nature.com/reprints).

**Publisher's note** Springer Nature remains neutral with regard to jurisdictional claims in published maps and institutional affiliations.

**Open Access** This article is licensed under a Creative Commons Attribution 4.0 International License, which permits use, sharing, adaptation, distribution and reproduction in any medium or format, as long as you give appropriate credit to the original author(s) and the source, provide a link to the Creative Commons license, and indicate if changes were made. The images or other third party material in this article are included in the article's Creative Commons license, unless indicated otherwise in a credit line to the material. If material is not included in the article's Creative Commons license and your intended use is not permitted by statutory regulation or exceeds the permitted use, you will need to obtain permission directly from the copyright holder. To view a copy of this license, visit <http://creativecommons.org/licenses/by/4.0/>.

© The Author(s) 2024